

## Maia X-ray fluorescence imaging: Capturing detail in complex natural samples

This content has been downloaded from IOPscience. Please scroll down to see the full text.

2014 J. Phys.: Conf. Ser. 499 012002

(<http://iopscience.iop.org/1742-6596/499/1/012002>)

View [the table of contents for this issue](#), or go to the [journal homepage](#) for more

Download details:

IP Address: 131.169.95.181

This content was downloaded on 12/11/2015 at 13:24

Please note that [terms and conditions apply](#).

## Maia X-ray fluorescence imaging: Capturing detail in complex natural samples

C G Ryan<sup>1</sup>, D P Siddons<sup>2</sup>, R Kirkham<sup>3</sup>, Z Y Li<sup>2</sup>, M D de Jonge<sup>4</sup>, D J Paterson<sup>4</sup>, A Kuczewski<sup>2</sup>, D L Howard<sup>4</sup>, P A Dunn<sup>3</sup>, G Falkenberg<sup>5</sup>, U Boesenberg<sup>5</sup>, G De Geronimo<sup>2</sup>, L A Fisher<sup>1</sup>, A Halfpenny<sup>1</sup>, M J Lintern<sup>1</sup>, E Lombi<sup>6</sup>, K A Dyl<sup>7</sup>, M Jensen<sup>3</sup>, G F Moorhead<sup>3</sup>, J S Cleverley<sup>1</sup>, R M Hough<sup>1</sup>, B Godel<sup>1</sup>, S J Barnes<sup>1</sup>, S A James<sup>4</sup>, K M Spiers<sup>4</sup>, M Alfeld<sup>5</sup>, G Wellenreuther<sup>8</sup>, Z Vukmanovic<sup>7,1</sup> and S Borg<sup>1</sup>

<sup>1</sup> CSIRO Earth Sciences and Resource Engineering, 26 Dick Perry Avenue, Kensington, WA 6151, Australia

<sup>2</sup> Brookhaven National Laboratory, Brookhaven, Upton NY, USA

<sup>3</sup> CSIRO Materials Science and Engineering, Normanby Road, Clayton VIC 3168, Australia

<sup>4</sup> Australian Synchrotron, Blackburn Road, Clayton VIC 3168, Australia

<sup>5</sup> Photon Science, DESY, Notkestr. 85, D-22603 Hamburg, Germany

<sup>6</sup> Centre for Environmental Risk Assessment and Remediation, University of South Australia, Building X, Mawson Lakes Campus, Mawson Lakes SA 5095, Australia

<sup>7</sup> Department of Applied Geology, Curtin University, GPO Box U1987, Perth, WA 6845, Australia

<sup>8</sup> European XFEL, Albert-Einstein-Ring 19, 22761 Hamburg, Germany.

E-mail: [chris.ryan@csiro.au](mailto:chris.ryan@csiro.au)

**Abstract.** Motivated by the challenge of capturing complex hierarchical chemical detail in natural material from a wide range of applications, the Maia detector array and integrated real-time processor have been developed to acquire X-ray fluorescence images using X-ray Fluorescence Microscopy (XFM). Maia has been deployed initially at the XFM beamline at the Australian Synchrotron and more recently, demonstrating improvements in energy resolution, at the P06 beamline at Petra III in Germany. Maia captures fine detail in element images beyond 100 M pixels. It combines a large solid-angle annular energy-dispersive 384 detector array, stage encoder and flux counter inputs and dedicated FPGA-based real-time event processor with embedded spectral deconvolution. This enables high definition imaging and enhanced trace element sensitivity to capture complex trace element textures and place them in a detailed spatial context. Maia hardware and software methods provide per pixel correction for dwell, beam flux variation, dead-time and pileup, as well as off-line parallel processing for enhanced throughput. Methods have been developed for real-time display of deconvoluted SXRF element images, depth mapping of rare particles and the acquisition of 3D datasets for fluorescence tomography and XANES imaging using a spectral deconvolution method that tracks beam energy variation.

### 1. Introduction

The design of the Maia detector array and imaging system has been motivated by the need to capture intricate spatial and chemical detail in complex natural samples. While the motivation for ever higher



spatial resolution in the development of X-ray microscopy is driven by the need to capture the finest structures, these details need to be interpreted within their larger spatial context. For instance, evidence for diffusion, reaction or crystallization along grain boundaries provides geologists with clues to process and timing. However, these textural and chemical clues must be seen within the context that the hosting structure provides. For example, areas which show evidence for infiltrating fluids and alteration may occur from the scale of inter-grain boundaries up to crustal scales spanning 12 orders of magnitude. If we concentrate on the goal of maximizing information content within the scale of geological samples presented for X-ray fluorescence mapping analysis (e.g. in the form of mineralogical thin-sections) then the textural clues are contained within spatial scales from a few cm down to the focussed X-ray beam size of  $\sim 1 \mu\text{m}$ . This presents a challenge of capturing detail over  $\sim 4$  orders of spatial scale.

An example of a common fine detail problem can be described as “needles in a haystack”. These are very rare particles or mineral phases, which are minute in size and may occur only at a rate of a few per square centimetre and challenge the spatial resolution of the X-ray microprobe. In geology, examples include rare gold particles sought in studies of ore genesis, rare resilient platinum group minerals that may survive in the Earth’s mantle for billions of years, elusive gold precipitates in plants growing over ore deposits or rare pre-solar condensates that may provide clues to early solar system formation if they can be identified. However, these objects may occur only at average concentrations of a few ppb, concentrated in a few sub-micron phases, located at unknown positions somewhere within the thin-section. X-ray fluorescence microscopy (XFM) is ideal for this type of analysis as it can detect and image a sub-micron particle at depth within a section.

Capturing detail over 4 orders of magnitude of spatial scale demands the ability to produce images of  $\sim 10^8$  pixels in practical time-scales, such as 3–10 hours (e.g. 0.1 to 0.4 ms per pixel). Scanning at this pixel rate demands an approach that eliminates read-out overheads. To obtain adequate counting statistics within each of these pixels at least for major/minor components (e.g.  $\sim 10^3$  counts) demands total detector count-rates of  $\sim 10$  M/s. The approach taken with the Maia detector has been to spread such high count-rates over a large number of detectors in an array, rather than attempt heroic count-rates in a small number of detectors with its inherent risk of serious pileup artefacts and degraded energy resolution. This has only been possible by making use of the large scale analogue circuit integration developments at Brookhaven National Laboratory [1].

A parallel goal of the Maia development has been to achieve high count-rates by maximizing total detector array solid-angle rather than increasing flux. In this way sample damage can be minimized. This has entailed design of Maia coordinated with the design of the XFM end-stations [2] at the Australian Synchrotron (AS). Its KB mirror end-station, with its large working distance of 69 mm provided little challenge. However, the coordinated design of Maia and its Xradia nanofocussing end-station demanded several design iterations to accommodate the 25 mm working distance of its diffractive optics. The Maia detector array uses an annular, “back-scattering” geometry, where the beam passes through the detector located upstream of the sample. The annular configuration enables a large solid-angle without imposing severe restrictions on sample size or the scale of scanning.

The challenge of data acquisition at count-rates up to or exceeding 10 M/s, with pixel times as short as 0.1 ms or less while avoiding readout overheads, was tackled by applying a nuclear physics approach to data acquisition using event-mode data collection with real-time processing. In addition, the real-time processing capability provides a platform in which established techniques for real-time spectral deconvolution can be applied, which paves the way for the display of deconvoluted element images in real-time.

This paper outlines the design and performance of the Maia detector array and imaging system as implemented for the XFM beamline at the AS in a coordinated endstation-detector design exercise. This paper will also present new improvements in Maia technology that are benefitting XFM analysis at the P06 beamline [3] at Petra III in Germany, which uses a new version of Maia with improved energy resolution. It also provides a discussion of the advantages and drawbacks of the annular geometry.

## 2. The Maia detector array and imaging system

The detector array comprises a  $20 \times 20$  array of  $1 \text{ mm}^2$  individual detectors with a central group ( $4 \times 4$ ) removed (figure 1) to accommodate the central Mo collimating tube for the passage of the X-ray beam through the detector [1,4]. A Mo mask grid over the array absorbs X-rays that may otherwise result in charge sharing between detectors [5]. A target-detector distance of 10 mm provides a total solid angle of 1.3 sr. Each detector is directly wire-bonded onto the inputs of 12 HERMES 32-channel custom applications specific integrated circuits (ASICs) providing pre-amplification, baseline restoration and 5-pole quasi-Gaussian pulse shaping to each detector channel [1,6]. Each HERMES channel drives an input of 12 SCEPTER 32-channel de-randomizer ASICs, which sample pulse-height (E) and time over threshold (T) for each detector pulse and provide a sample-and-hold function for digitization [7], multiplexed into 4 banks of high-speed 14-bit synchronous ADC pairs. A field-programmable gate-array (FPGA) in the detector head packages detected events into data representing events  $\{n, E, T\}$ , for detector channels 'n', and transmits them over a dedicated 8 Gb/s quad-channel fibre optic link to the real-time processing sub-system located outside the beamline enclosure [4].

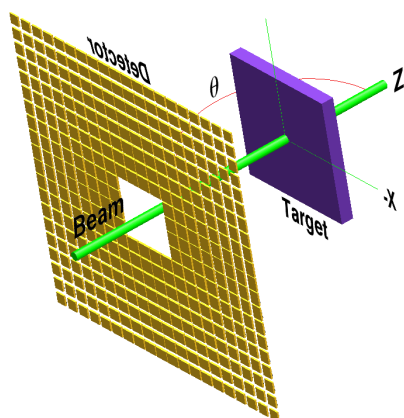


Figure 1 The Maia detector annular array comprises a  $20 \times 20$  array of  $1 \text{ mm}^2$  silicon detector elements, with a central group ( $4 \times 4$ ) removed to accommodate the passage of the X-ray beam (see detector fabrication details in ref: [1]). The plane of the array is 10 mm from the focussed spot on target. The size of the detectors depicted here in perspective, which diminish towards the outer perimeter, reflects the effective size after masking to avoid charge-sharing between detectors (the mask is detailed in ref: [5]).

The real-time processing sub-system uses a CSIRO HYMOD processor. It comprises a FPGA, which provides pipelined parallel processing of the event stream, and a co-processor to handle control and display client requests and event transmission over Ethernet [4]. A new event can be clocked through the FPGA each clock cycle at up to 50 M/s. In parallel, the HYMOD system samples pulses from the upstream and downstream ion-chamber V-to-F units to count beam flux on a per pixel basis and tracks stage encoder position to enable each output event record to be tagged by stage position. The event processing pipeline comprises: (i)  $\pm 0.5$  dither applied to E to reduce subsequent aliasing effects, (ii) linearization correction, (iii) linear gain trimming to match E and T across detector channels, (iv) energy calibration mapping, (v) pile-up rejection, (vi) individual detector count-rate monitoring, (vii) dead-time and pileup monitoring across the array, and (viii) real-time element image accumulation triggered directly by sample stage motion. Processed events, optionally sub-sampled ('throttled') on the basis of energy, are also logged to disk, tagged by sample stage pixel coordinates with incident and transmitted flux counts accumulated in that pixel. Throttling reduces the size of raw data files through suppression of strong element lines or scatter peaks.

## 3. Treating spectral complexity

Many applications, especially those in the environmental, planetary and geological sciences, are characterized by complex synchrotron XRF spectral content with numerous overlaps between elements. The analysis of complex SXRF spectra is well developed, typically using a least-squares fitting approach with X-ray line yields based on a detailed model of the sample (e.g. [8,9]). The Dynamic Analysis (DA) method is based on an extension of this approach to imaging. In the limit of a linear least-squares fit, where non-linear terms for peak width, tailing and energy calibration adjustment have been constrained by prior measurement (or prior non-linear fit iterations), the solution

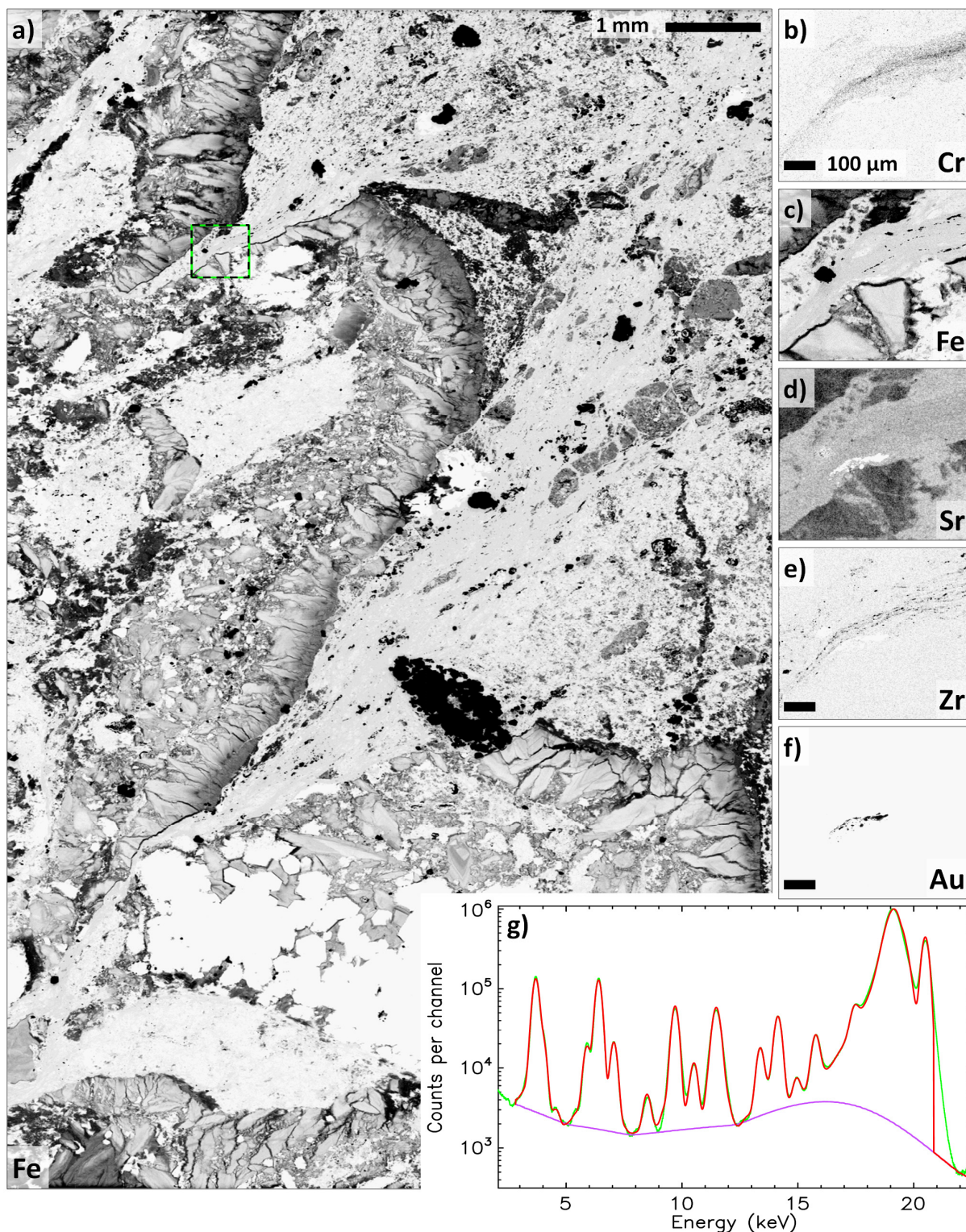


Figure 2 Maia images of a thin-section from the western shear zone of the Sunrise Dam deposit, Western Australia acquired on the P06 beamline; a) large area Fe image (4050 x 8000 pixels, 8 x 16 mm<sup>2</sup>) showing a zoom in area (box top left); images (0.61 x 0.70 mm<sup>2</sup>) from area in (a) for b) Cr, c) Fe, d) Sr, e) Zr and f) Au; and g) total spectrum for detector #124 for the central portion of the scan (overlaid by GeoPIXE fit and background), for total detector count-rate of 4 M/s ( $\tau = 1 \mu\text{s}$ ).

of the fitting problem using the function linearization method [10] reduces to the solution of a set of simultaneous equations. In matrix form, these equations can be rearranged into the form of element intensities given by a matrix transformation of the spectrum of interest [11].

Using a fundamental parameters approach to SXRF analysis, the element intensities can be related to concentration, which results in a matrix transformation directly from input spectrum to element concentration vector [12]. In the Maia case, the model includes the effects of the Mo mask on individual detector solid-angles and the changing spectral relative intensities across the array, as an extension of the layered sample model in the GeoPIXE software [5,13,14]. The model produces a set of relative sensitivity factors (RSFs) for the individual detectors across the array reflecting changing distance, angle, absorption paths and intrinsic efficiency. Application of the RSF approach enables any sub-set of detectors, or individual detectors, to be used in a particular analysis. An example is the mapping of particle depth, which makes use of contrasting self absorption in the sample experienced by radial groupings of inner and outer detector elements [15].

The DA method can be used for rapid spectrum processing [11,15,16]. However, this approach also can be used to map each event in turn onto its element concentration contributions [17]. Some of these contributions are negative, which is how overlap and background subtraction are accomplished [12]. In the Maia detector processor, these contributions are accumulated for all events in the current image pixel in what reduces to a simple lookup-accumulate operation implemented in the HYMOD FPGA [14]. When the stage moves out of the pixel, the accumulator is read-out as a concentration record, which is displayed immediately by the real-time display client.

#### **4. Application methods using Maia**

The key capabilities of the Maia detector system that enable the high throughput of the XFM beamline are (i) transit times per pixel (referred to below as “dwell time”) down to 50  $\mu\text{s}$  [14], (ii) close detection geometry providing a solid angle of 1.3 sr [5], (iii) high sustained count rates, normally up to 12 M/s, (iv)  $100 \times 100 \text{ mm}^2$  scan range and image area ( $600 \times 300 \text{ mm}^2$  on the XFM large format stage), (v) image pixel count beyond  $10^8$  pixels, (vi) real-time spectral deconvolution and image display, and (vii) moderate inelastic scattering signal that provides good collective images of light elements [18], especially useful for biological samples [19-22]. Typically, pixel times and image areas are not generally a limitation, and these are chosen to suit a particular application. This has enabled a range of application methods at the XFM beamline and most are finding application at the P06 beamline at Petra III.

##### **4.1. Large area mapping**

Scans of complex natural samples can be performed over  $100\text{--}200 \text{ mm}^2$  at full spatial resolution of  $2 \mu\text{m}$  on the XFM KB endstation. Larger areas to  $10 \text{ cm}^2$  are typically done at  $4\text{--}6 \mu\text{m}$  resolution. Typical image size is  $10\text{--}100 \text{ M}$  pixels acquired over  $2\text{--}10$  hours [14]; the largest image to date is  $620 \text{ M}$  pixels. Using a collimated beam, larger objects, such as works of art, have been imaged at  $50\text{--}100 \mu\text{m}$  resolution [18] over areas up to  $600 \times 300 \text{ mm}^2$ . This method has been applied to studies in the earth [23-30], planetary [31], environmental [32,33], medical [19,34], biological [20-22,35-41] and material [42] sciences as well as cultural heritage [18,43]. A similar capability has been established on the P06 beamline (e.g. figure 2).

##### **4.2. Survey and detail mapping**

Large area mapping can be performed at small dwell time per pixel to provide overview survey images (e.g.  $6 \text{ M}$  pixels in 1 hour) in major and minor elements from which smaller detail areas are selected for scanning at increased dwell time and/or spatial resolution [24,33,15]. Real-time imaging enables these selections to be made during survey image acquisition.

### 4.3. Depth mapping

The Maia detector array subtends a large range of takeoff angles for X-rays exiting the sample surface, with the angle between the sample normal and ray to the centre of individual detectors varying between  $13.9^\circ$  and  $52.6^\circ$ . This makes the outer detectors much more sensitive to self-absorption for X-rays from a particle at depth in a sample than the inner detectors. Such a difference can be harnessed to provide an imaging contrast based on particle depth and also a quantitative measure of depth for discrete identified particles [15]. This approach has been used to locate rare gold precipitates in eucalyptus leaves [29] (e.g. figure 3) and rare phases including platinum group minerals in mantle derived rocks and meteorites [15].

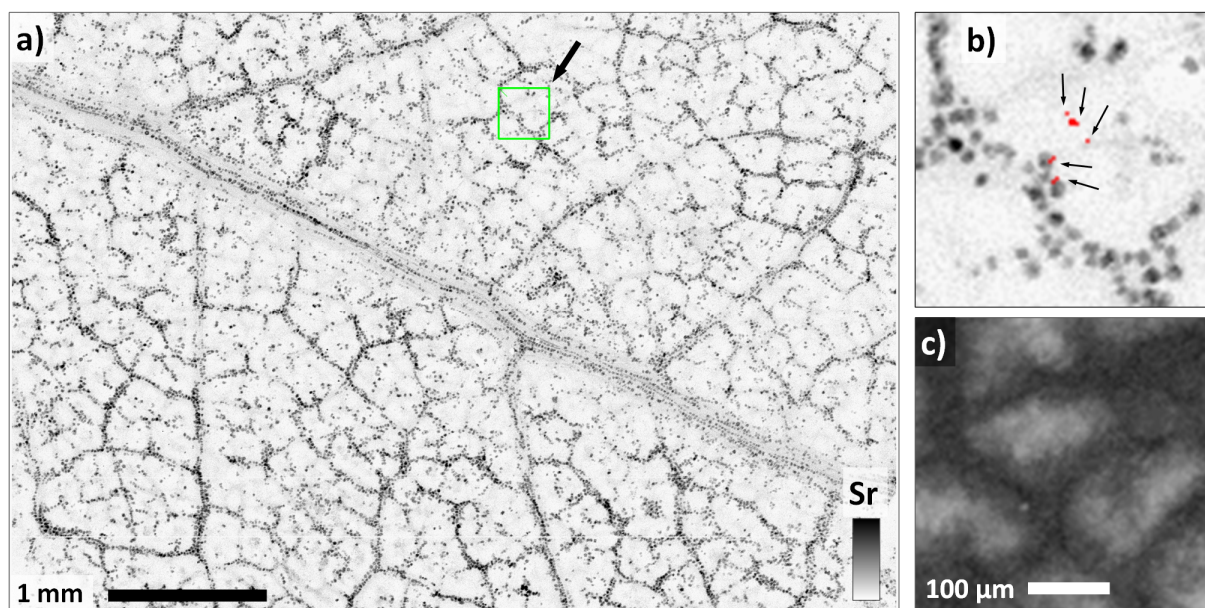


Figure 3 Maia XFM images of a portion of Eucalyptus leaf showing a) Sr distribution ( $5.6 \times 3.8 \text{ mm}^2$ ,  $2814 \times 1894$  pixels) showing oxalate crystals (Sr is a proxy for Ca), b) zoom in on Sr map ( $0.36 \times 0.36 \text{ mm}^2$ , from box in (a)) showing Au grains (red) indicated by arrows (two attached to oxalate crystals), and c) Compton scattering map (see ref: [29]).

### 4.4. XANES image stacks and XANES tomography

The capability of the Maia detector for imaging to around  $10^8$  pixels paves the way for 3D imaging modalities, such as XANES imaging, where the production of images up to  $\sim 10^6$  pixels can be repeated  $\sim 10^2$  times with changing beam energy through an absorption edge from which chemical state images can be projected [25,43,45]. Repeated single slice tomography at energies across an absorption edge also can be used to provide cross-sectional chemical state images [48].

**4.4.1. DA method for XANES imaging.** The DA method provides a linear least squares fit result at real-time processing speed. The model includes all excited X-ray lines, a background term and elastic and inelastic scattering peaks, where inelastic scattering is treated using an empirical function [44]. The method has been extended to XANES imaging by shifting the centroids of the elastic and inelastic peaks to track the changing beam energy. The full non-linear fit is performed on the SXRF spectrum at the top beam energy for the XANES scan, in which the shape of the background and the inelastic scattering distributions are determined. Then a series of DA matrices are generated as the beam energy is reduced according to the method of Ryan *et al.* [12,14] with the elastic and inelastic peaks shifted to track the change in beam energy. During processing of the event stream, the lookup table operation first selects the correct DA matrix for the beam energy and then selects the matrix column based on event X-ray energy to increment a 2D result array indexed by XY position repeated over beam energy.

The benefit of this approach are XANES spectra for each XY with subtraction of contributions due to scattering, background and other elements, including those experiencing their own edge structure within the XANES beam energy range [45]. This method is part of the GeoPIXE software suite [46].

#### 4.5. 3D fluorescence tomography

Large pixel count can be recast as a large voxel count for 3D fluorescence tomography, particularly where matrix absorption is low. 5  $\mu\text{m}$  tomographic data have been acquired using a KB mirror pair with  $\sim 2 \mu\text{m}$  resolution over  $\sim 1 \text{ mm}$  specimens [37]. Single-slice data can be obtained from highly radiation-sensitive specimens, such as fresh and fully hydrated plant roots, in a matter of minutes [20,21,38,39]. Measurement of the Ge distribution in an intact rice grain with 2  $\mu\text{m}$  voxels over 2–3 mm dimensions utilized high-definition 2D fluorescence tomography, with 2001 projections and a measurement time of the order of 3 hours [22] (figure 4a). Maia has enabled fluorescence tomography to become routine; however the ability to measure ever larger specimens now demands a general solution to the self absorption problem (see ref: [47] and references therein).

### 5. Maia detector performance

Recent tests of the Maia system showed that the measurements of the RSFs across the array for thin standard metal foils [49] show agreement with the model values at better than 3% relative standard deviation [50]. Further tests, aimed at demonstrating quantitative element imaging over a wide count-rate range, used these metal foils and a wide range of beam flux to produce total count-rates from 0.1 to 12 M/s, which corresponds to  $\sim 0.1$  to  $\sim 10\text{--}40 \text{ k/s}$  in individual detectors. Pileup rejection used the E-T behaviour to identify and reject pileup events, as outlined by Dragone *et al.* [7], and each event T provided a measure of dead-time. Accounting for pile-up rejection and dead-time losses enabled quantitative analysis of the metal standards using GeoPIXE consistent to within a relative standard deviation of 0.2% for count-rates from 0.1 to 12 M/s [50]. Interestingly, total dead-time was only 5% at a total count-rate of 12 M/s (1  $\mu\text{s}$  peaking time  $\tau$ ). Maximum count-rate is limited at present by the selected SCEPTER clock to 36 M/s.

Ongoing development of the Maia detector has yielded improvements in the energy resolution and aided the detection of lower energy X-rays. The new model 384B, tested recently at the P06 beamline at Petra III, achieved an energy resolution for Mn  $K\alpha$  with an average FWHM of 240 eV across the array, using a HERMES peaking time of 4  $\mu\text{s}$ , and enabled X-ray detection down to 2.0 keV. Figure 2g shows a typical Maia detector spectrum at a total count-rate of 4 M/s (with overlaid GeoPIXE fit and SNIP background [51]). Normalization to flux counts on a pixel by pixel basis is now routine, which helps to eliminate the effects of pixel dwell fluctuations caused by scanning stage motor speed variation.

### 6. The annular geometry

The annular configuration enables a large detection solid-angle without imposing restrictions on the size of samples or the scale of scanning. This approach enables scanning of virtually any sample size while maintaining large solid-angle. Sample areas as large as  $\sim 0.6 \times 0.3 \text{ m}^2$  (e.g. works of art) can be accommodated at the XFM beamline [18]. The cost of this approach is increased scatter compared to a small solid-angle detector located at  $90^\circ$  along the direction of typical horizontal beam polarization. As shown in figure 4c, departure from  $90^\circ$  results in at least a 30-fold increase in background for a small solid-angle silicon drift detector (SDD) [52]. Spectral background at  $90^\circ$  remains limited by the combined effects of multiple scattering in the sample and environment as well as incomplete charge collection background in the detector.

However, pursuing large solid-angle tends to wash out the advantage of the  $90^\circ$  geometry, with only a marginal penalty for choosing the annular geometry ( $\theta=180^\circ$ ); scatter increases by less than a factor of 3 for Maia between  $90^\circ$  and  $180^\circ$  (figure 4b). The great increase in detector solid-angle afforded by the close annular geometry more than compensates for this slight disadvantage allowing a 200-fold increase in counting statistics in this example, which yields improved detection limits and is

crucial for obtaining the high level of counting statistics needed for quality imaging. Figure 5 illustrates that large detector solid angle helps avoid inadequate counting statistics, which can degrade effective image spatial resolution well beyond actual beam resolution.

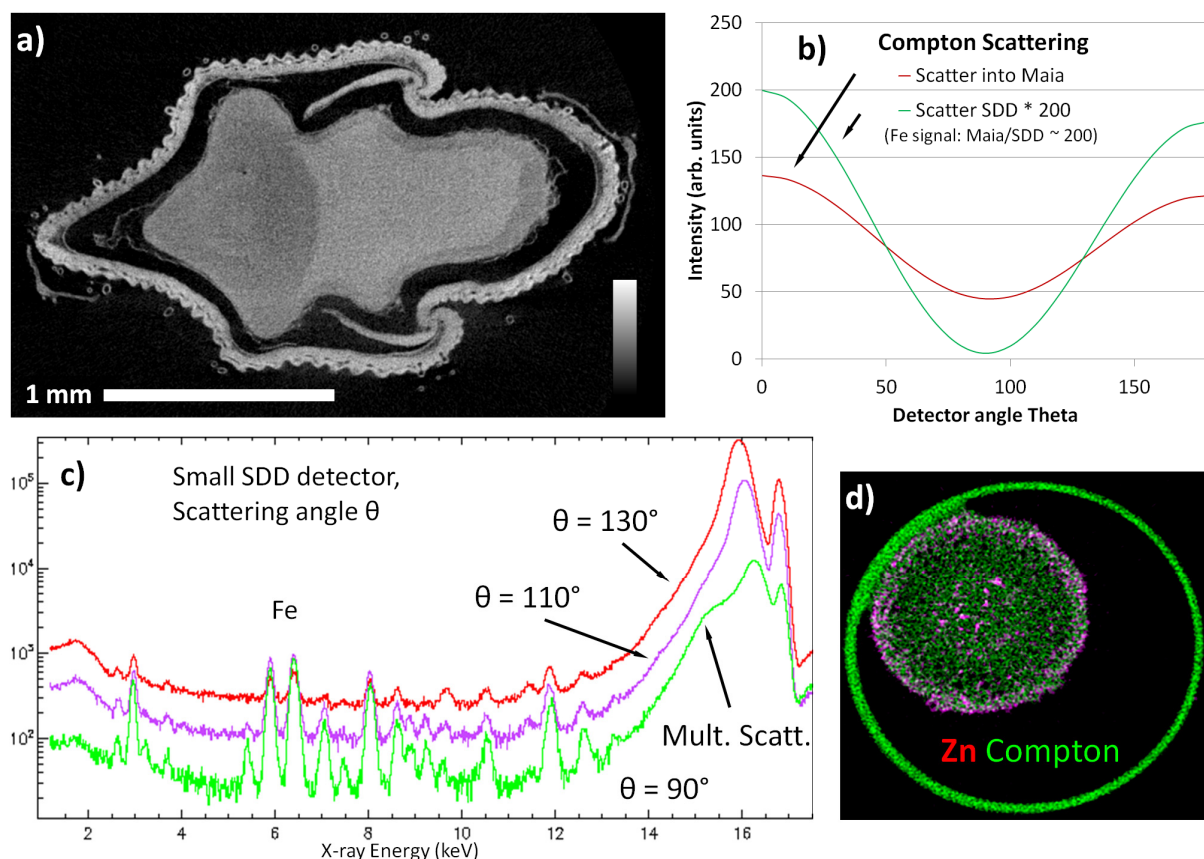


Figure 4 a) Maia Compton scattering tomography data reconstructed to show a section through a rice grain (4.5 mm scan {2291 pixels} at 2001 projections, see ref: [22]); b) angular distribution of Compton scattering for a small SDD detector ( $\Omega=6.2$  msr) ignoring multiple scattering (green) and the Compton angular distribution using a Maia detector ( $\Omega=1.3$  sr, scaled down x200 in red) as a function of detector angle theta (annular geometry at  $180^\circ$ ); c) spectra for a thin NBS 1832 standard normalized to fluence using a small SDD detector as a function of detector angle  $\theta$  [52], and d) reconstruction of Maia fluorescence tomography data for a section through a capillary tube containing a rootlet (see ref: [21]) showing the tube and root imaged using Compton scattering (green).

A final point in this discussion is the observation that the scatter signal has proven very useful in its own right as a means to image the structure of biological samples as a collective proxy for light elements. Compton scattering from light elements is dominant in biological samples, illustrated in figures 4a,d and 3c. Numerous examples of Maia imaging of light elements using scattering can be found elsewhere (e.g. [19-22,40]).

## 7. Application examples

The Sunrise Dam Gold Mine contains ~14 M oz gold and is the largest known deposit in the Laverton Tectonic Zone of the Eastern Goldfields province, Western Australia [53]. Gold is hosted in shear-parallel flat veins, steep stockwork veins and hydrothermal breccia bodies. The veins typically have quartz-carbonate mineralogy with sericite-sulphide alteration of the surrounding wall rock. The majority of gold is hosted within the veins with little evidence for gold within the wall rock [53]. Maia

XFM maps of a deformed Au-bearing quartz-carbonate vein from the western shear zone of Sunrise Dam (figure 2) shows evidence for a complex deformation and alteration history associated with multiple Au populations [54]. Chemical zonations within the carbonate minerals indicate multiple phases of vein growth and subsequent deformation and alteration [55]. Coarse Au is hosted within the fractured vein, while a rare, finely textured Au population is hosted in sericite altered shear zones on the boundary between the vein and the wall rock (figure 2f). These sheared, sericite rich zones, are characterised by abundant hydrothermal zircon and an elevated Cr content (figure 2b, indicating presence of fuchsite, a common alteration phase at Sunrise Dam). The contrast in size between the Au populations in the vein and sheared boundary between the vein and wall rock may indicate multiple Au deposition events, or (more likely) the gold grain size is controlled by the rheology of the host phases and space available for growth.

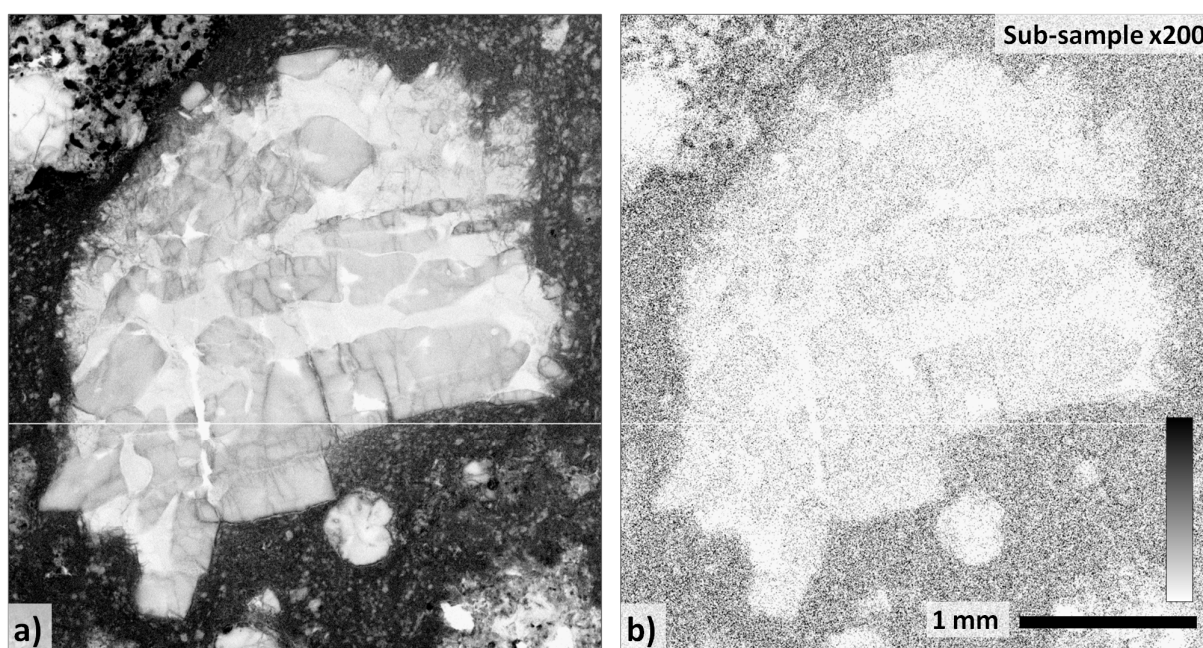


Figure 5 a) Maia Fe image of a single chondrule in an Allende meteorite sample ([31], see description in ref: [15]); and b) the same data-set sub-sampled x200 to illustrate how lower counting statistics degrades image quality, perceived detail and effective spatial resolution.

Geochemical sampling of vegetation above known gold ore bodies has been shown by Lintern [56] to exhibit anomalously high Au concentrations. Hence, the uptake of metals by vegetation has potential as a mineral exploration technique. In arid regions of Australia, species of Eucalyptus and Acacia can develop root systems that tap water and dissolved metals down to depths of ~40 m. However, the mechanism for Au enrichment in vegetation is unknown and it has been difficult to distinguish natural uptake from surface contamination. A recent study by Lintern *et al.* [29] combined field sampling of fresh Eucalyptus leaves and Maia XFM imaging to locate and image rare gold precipitates located within the leaves. The Freddo gold prospect, Western Australia, was selected as a site to investigate the potential mechanisms for the chemical transport of Au and uptake by plants with the results compared with laboratory studies using seedlings of native Eucalyptus and Acacia dosed with Au. The Freddo deposit is undisturbed by mining activity and has no known sources of surface contamination. The sub-economic ore body is concealed beneath ~30 m of barren overburden. Nevertheless, gold precipitates were located using XFM in numerous leaf samples; the speed of Maia imaging enabled 60 leaf discs samples (6 mm in diameter) to be imaged at 2  $\mu\text{m}$  resolution (e.g. figure 3), punched from 20 leaves selected from high Au samples (~10–50 ppb Au bulk average). Some Au

particles were observed to be associated with Ca oxalate crystals (figure 3b), which parallels the associations seen between Ca and Au in calcrete in arid areas, and suggests that Au and Ca also share a common biological pathway in these systems [29].

## 8. Conclusions

The real-time event-by-event processing approach used in the Maia system relaxes constraints on the selection of dwell time per pixel. Image sizes and pixel dwell can be chosen to suit the needs of the application and to provide adequate counting statistics, with pixel size set generally by the beam size. Obtaining adequate counting statistics, especially for trace elements, is aided by the large collection solid-angle of Maia and the pulse handling and real-time processing modules, which can handle event rates beyond 20 M/s. Alternatively, large solid-angle and small dwell times can be used to minimize dose per pixel and help avoid radiation damage induced chemical changes to samples. Combined with the reliability and stability of the XFM beamline, the result is a flexible microanalytical tool for large area, high definition mapping at  $\sim 2 \mu\text{m}$  spatial resolution to around  $10^8$  pixels, and for 3D imaging modalities, such as XANES chemical state imaging and 3D fluorescence tomography. Early results at the P06 beamline show that similar flexibility and performance are being provided by the new Maia 384B detector, which exhibits improved energy resolution, yielding high definition elemental maps at  $\sim 0.5 \mu\text{m}$  spatial resolution.

In user applications, Maia is proving especially useful for large scale, high definition XFM imaging and locating rare minute metal particles in geological and biological samples. The large detector array, with a wide range of X-ray take-off angles, also provides sensitivity to the depth of features within a sample, which has been utilized to provide an imaging depth contrast. Maia large area mapping was exploited to capture the complexity of chemical and physical processes at play in the Sunrise Dam deposit and their influence on the mobility and deportment of gold in the ore. Rare gold precipitates were observed in the leaves of Eucalypts growing above an undisturbed ore body concealed beneath  $\sim 30$  m of cover. The results provide a sound basis for the application of gold in selected vegetation species as a technique for the exploration for gold in concealed ore deposits.

## Acknowledgements

This research was undertaken on the X-ray fluorescence microscopy beamline at the Australian Synchrotron, Victoria, Australia, and the Hard X-ray Micro/Nano-Probe beamline P06, Petra III, DESY, Germany. The authors wish to thank Stefan Vogt for his help acquiring SDD standards spectra.

## References

- [1] Siddons D P, Kirkham R, Ryan C G, De Geronimo G, Dragone A, Kuczewski A J, Li Z Y, Carini G, Beuttenmuller R, Elliott D *et al.* 2013 Maia X-ray Microprobe Detector Array System *these proceedings*
- [2] Paterson D, de Jonge M D, Howard D L, Lewis W, McKinlay J, Starritt A, Kusel M, Ryan C G, Kirkham R, Moorhead G, Siddons D P 2011 *AIP Conf. Proc.* **1365** 219-222
- [3] Schroer C G, Kurapova O, Patommel, Boye P, Feldkamp J, Lengeler B, Schwab A, Stephan S, Falkenberg G, Wellenreuther G and Reimers N 2010 *Nucl. Instr. Meth. A* **616** 93
- [4] Kirkham R, Dunn P A, Kucziewski A, Siddons D P, Dodanwela R, Moorhead G, Ryan C G, De Geronimo G, Beuttenmuller R, Pinelli D *et al.* 2010 *AIP Conf. Proc.* **1234** 240-243
- [5] Ryan C G, Kirkham R, Hough R M, Moorhead G, Siddons D P, de Jonge M D, Paterson D J, De Geronimo G, Howard D L and Cleverley J S 2010 *Nucl. Instr. Meth. A* **619** 37-43
- [6] De Geronimo G, O'Connor P, Beuttenmuller R H, Li Z, Kuczewski A J and Siddons D P 2003 *IEEE Transactions on Nuclear Science* **50** 885-891
- [7] Dragone A, De Geronimo G, Fried J, Kandasamy A, O'Connor P and Vernon E 2005 *IEEE Nuclear Science Symposium Conference Record* **2** 914-918
- [8] Ryan C G, Etschmann B E, Vogt S, Maser J, Harland C L, van Achterbergh E and Legnini D 2005 *Nucl. Instr. Meth. B* **231** 183-188

- [9] Solé V A, Papillon E, Cotte M, Walter Ph, Susini J 2007 *Spectrochimica Acta B* **62** 63-68
- [10] Bevington P R 1969 *Data reduction and error analysis for the physical sciences* (McGraw-Hill, New York)
- [11] Ryan C G and Jamieson D N 1993 *Nucl. Instr. Meth. B* **77** 203-214
- [12] Ryan C G 2000 *International Journal of Imaging Systems and Technology* (special issue on "Advances in Quantitative Image Analysis") **11** 219-230
- [13] Ryan C G, Cousens D R, Sie S H, Griffin W L, Suter G F and Clayton E 1990 *Nucl. Instr. Meth. B* **47**, 55-71
- [14] Ryan C G, Siddons D P, Kirkham R, Dunn P A, Kuczewski A, Moorhead G, De Geronimo G, Paterson D J, de Jonge M D, Hough R M *et al.* 2010 *X-Ray Optics and Microanalysis, AIP Conference Proc.* **1221** 9-17
- [15] Ryan C G, Siddons D P, Kirkham R, Li Z Y, de Jonge M D, Paterson D, Cleverley J S, Kuczewski A, Dunn P A, Jensen M *et al.* 2013 The Maia detector array and X-ray fluorescence imaging system: Locating rare precious metal phases in complex samples (SPIE conference on X-ray Nanoimaging, San Diego Aug 2013) *AIP Conf. Proc.* in press.
- [16] Alfeld M 2013 The processing of large, heterogeneous data sets acquired for XRF imaging *ICXOM conference presentation and abstract*
- [17] Ryan C G, Jamieson D N, Churms C L and Pilcher J V 1995 *Nucl. Instr. Meth. B* **104** 157-165
- [18] Howard D L, de Jonge M D, Lau D, Hay D, Varcoe-Cocks M, Ryan C G, Kirkham R, Moorhead G, Paterson D and Thurrowgood D 2012 *Analytical Chemistry* **84** 3278-3286
- [19] Zhang J Z, Bryce N S, Siegele R, Carter E A, Paterson D, de Jonge M D, Howard D L, Ryan C G, Hambley T W 2012 *Integrated Biology* **4** 1072-1080
- [20] Kopittke P M, Menzies N W, de Jonge M D, McKenna B A, Donner E, Webb R I, Paterson D, Ryan C G, Glover C J and Lombi E 2011 *Plant Physiology* **156** 663-673
- [21] Lombi E, de Jonge M D, Donner E, Kopittke P M, Howard D L, Kirkham R, Ryan C G and Paterson D 2011 *PLoS One* (Public Library of Science) **6(6)** e20626
- [22] Carey A-M, Lombi E, Donner E, de Jonge M D, Punshon T, Jackson B P, Guerinot M L, Price A H, Meharg A A 2012 *Analytical and Bioanalytical Chemistry* **402** 3275-3286
- [23] Lintern M, Hough R and Ryan C 2012 *J. Geochem. Explor.* **112** 189-205
- [24] Barnes S, Godel B, Locmelis M, Fiorentini M, Ryan C 2011 *Aust. J. Earth Sciences* **58** 691-709
- [25] Etschmann B E, Ryan C G, Brugger J, Kirkham R, Hough R M, Moorhead G F, Siddons D P, De Geronimo G, Kuczewski A, Dunn P A, *et al.* 2010 *American Mineralogist* **95** 884-887
- [26] Brugger J, Pring A, Reith F, Ryan C G, Etschmann B, Liu W, O'Neill B, Ngothai Y 2010 *Radiation Physics and Chemistry* **79** 151-161
- [27] Hough R M, Noble R R P, Butt C R M, Ryan C G, Lintern M J, Reddy S M, Paterson D, de Jonge M D 2010 *Smart Science For Exploration And Mining* **1-2** 716-718
- [28] Cleverley J S, Hough R, Ryan C, Maas R, Blake K, Nugus M 2010 *Smart Science For Exploration And Mining* **1-2** 213-215
- [29] Lintern M, Anand R, Ryan C, Paterson D 2013 *Nature Communications* **4** 2614 (<http://dx.doi.org/10.1038/ncomms3614>)
- [30] Barnes S J, Godel B, Ryan C G 2011 *Mineralogical Magazine* **75** 489
- [31] Dyl K A, Cleverley J S, Bland P A, Ryan C G and Hough R M 2013 Trace element mapping of carbonaceous chondrites Allende (CV3-Oxidized) and Vigarano (CV3-Reduced) at 2-micron resolution over centimetre-scales *Geochimica et Cosmochimica Acta* submitted
- [32] Padovan A, Munksgaard N, Alvarez B, McGuinness K, Parry D, Gibb K 2012 *Hydrobiologia* **687** 275-288
- [33] Donner E, Ryan C G, Howard D L, Zarcinas B, Scheckel K G, McGrath S P, de Jonge M D, Paterson D, Naidu R, Lombi E 2012 *Environmental Pollution* **166** 57-64
- [34] Myers D E, Ryan C G, Kirkham R, Paterson D, Moorhead G, Dunn P A, Siddons D P, de Jonge M D, Howard D L, De Geronimo G *et al.* 2010 *Injury* **41** (supplement 1) S30-S31
- [35] Lombi E, Smith E, Hansen T H, Paterson D, de Jonge M D, Howard D L, Persson D P, Husted

- S, Ryan C and Schjoerring J K 2011 *J Experimental Botany* **62** 273–282
- [36] Lye J C, Hwang J E C, Paterson D, de Jonge M D, Howard D L, Burke R 2011 *PLoS One* **6** e26867-1 - e26867-8
- [37] McColl G, James S A, Mayo S, Howard D L, Ryan C G, Kirkham R, Moorhead G F, Paterson D, de Jonge M D, Bush A I 2012 *PLoS ONE* **7** e32685-1 - e32685-4
- [38] Kopittke P M, de Jonge M D, Menzies N W, Wang P, Donner E, McKenna B A, Paterson D, Howard D L and Lombi E 2012 *Plant Physiology* **159** 1149–1158
- [39] Wang P, Menzies N W, Lombi E, McKenna B A, de Jonge M D, Donner E, Blamey F P C, Ryan C G, Paterson D J, Howard D L *et al.* 2013 *Science of the Total Environment* **463-464** 131–139
- [40] Howell N, Lavers J, Uematsu S, Paterson D, Howard D L, Spiers K M, de Jonge M D, Garrett R, Banati R 2013 High resolution X-Ray fluorescence microscopic analysis of breast feathers from two species of Procellariiformes, the Flesh-footed Shearwater (*Puffinus carneipes*) and the Streaked Shearwater (*Calonectris leucomelas*) *Integrative Biology* submitted
- [41] Lombi E, de Jonge M D, Donner E, Ryan C G, Paterson D 2011 *Anal. Bioanal. Chem.* **400** 1637-1644
- [42] Macdonald D, Rougieux F, Mansoulie Y, Tan J, Paterson D, Howard D L, de Jonge M D and Ryan C G 2010 *Phys. Status Solidi A* **207** 1807-1810
- [43] Monico L, Janssens K, Alfeld M, Vanmeert F, Falkenberg G, Ryan C G, Howard D L, Cotte M, Miliani C 2013 Van Gogh and alteration of chrome yellow pigments: new Cr- speciation studies using the Maia X-ray detector *ICXOM conference presentation and abstract*
- [44] van Gysel M, Lemberge P, van Espen P 2003 *X-ray Spectrometry* **32** 139
- [45] Spiers K M, pers. comm., manuscript in prep.
- [46] GeoPIXE software suite (<http://nmp.csiro.au/GeoPIXE.html>)
- [47] de Jonge M D and Vogt S 2010 *Current Opinion in Structural Biology* **20** 606–614
- [48] de Jonge M D, pers. comm., manuscript in prep.
- [49] Micromatter XRF calibration standards (MICROMATTER 4004 Wesbrook Mall, Vancouver, British Columbia, V6T 2A3, Canada) (<http://www.micromatter.com>)
- [50] Ryan C G, Siddons D P, Kirkham R, Paterson D J, de Jonge M D *et al.* Maia X-ray fluorescence imaging system: Real-time methods, imaging performance and applications, in prep.
- [51] Ryan C G, Clayton E, Griffin W L, Sie S H and Cousens D R, 1988, *Nucl. Instr. Meth. B* **34** 396-402
- [52] Vogt S, Pers. Comms.
- [53] Yardley B W D and Cleverley J S 2013 The role of metamorphic fluids in the formation of ore deposits, in *Ore Deposits in an Evolving Earth* eds. Jenkin G R T, Lusty P A J, McDonald I, Smith M P, Boyce A J and Wilkinson J J (Geological Society, London) *Special Publications* **393** (<http://dx.doi.org/10.1144/SP393.5>)
- [54] Cleverley J S, Hough R M, Ryan C G, Borg S 2011 *Let's Talk Ore Deposits* **1-2** 572-574
- [55] Halfpenny A, Fisher L, Hough R, Cleverley J 2013 *12th SGA Biennial Meeting Proc. Mineral Deposit Research for a High-Tech World* **3** 1255-1258
- [56] Lintern M J 2007 *Geochem. Exploration Environ. Anal.* **7** 249–266